



Alexander E.J. Hoffman, Jelle Wieme, Sven M.J. Rogge, Louis Vanduyfhuys and Veronique Van Speybroeck*

The impact of lattice vibrations on the macroscopic breathing behavior of MIL-53(Al)

<https://doi.org/10.1515/zkri-2018-2154>

Received November 30, 2018; accepted January 28, 2019; published online February 14, 2019

Abstract: The mechanism inducing the breathing in flexible metal-organic frameworks, such as MIL-53(Al), is still not fully understood. Herein, the influence of lattice vibrations on the breathing transition in MIL-53(Al) is investigated to gain insight in this phenomenon. Through solid-state density-functional theory calculations, the volume-dependent IR spectrum is computed together with the volume-frequency relations of all vibrational modes. Furthermore, important thermodynamic properties such as the Helmholtz free energy, the specific heat capacity, the bulk modulus, and the volumetric thermal expansion coefficient are derived via these volume-frequency relations using the quasi-harmonic approximation. The simulations expose a general volume-dependency of the vibrations with wavenumbers above 300 cm^{-1} due to their localized nature. In contrast, a diverse set of volume-frequency relations are observed for vibrations in the terahertz region ($<300\text{ cm}^{-1}$) containing the vibrations exhibiting collective behavior. Some terahertz vibrations display large frequency differences over the computed volume range, induced by either repulsion or strain effects, potentially triggering the phase transformation. Finally, the impact of the lattice vibrations on the thermodynamic properties is investigated. This reveals that the closed pore to large pore phase transformation in MIL-53(Al) is mainly facilitated by terahertz vibrations inducing rotations of the organic linker, while the large pore to closed pore phase transformation relies on two framework-specific soft modes.

Keywords: density-functional theory; metal-organic frameworks; phase transformation; thermodynamic properties; vibrational spectroscopy.

*Corresponding author: Veronique Van Speybroeck, Center for Molecular Modeling, Ghent University, Technologiepark 46, 9052 Zwijnaarde, Belgium, E-mail: veronique.vanspeybroeck@ugent.be
Alexander E.J. Hoffman, Jelle Wieme, Sven M.J. Rogge and Louis Vanduyfhuys: Center for Molecular Modeling, Ghent University, Technologiepark 46, 9052 Zwijnaarde, Belgium

Introduction

Present-day challenges such as global warming and energy supply have revealed a dire need for newly designed functional materials. Metal-organic frameworks (MOFs), also called porous coordination polymers, are a class of nanoporous materials potentially able to offer solutions to these challenges [1, 2]. MOFs are hybrid materials containing metal complexes connected with organic linkers. The intrinsic organic-inorganic nature of these crystalline frameworks has led to the construction of many thousands of MOFs [3] and even more hypothetical ones [4] with different dimensionalities. This variety is the key ingredient in finding suitable materials for energy-related applications [5], such as gas separation [6], chemical sensing [7], and heterogeneous catalysis [8].

The interplay of organic and inorganic moieties allows some MOFs to exhibit a high degree of structural flexibility without losing their crystallinity, so-called soft porous crystals [9–12]. A specific type of framework flexibility, called breathing, causes a large change in unit cell volume through the transformation from a large pore (LP) phase to a closed pore (CP) phase. This breathing behavior is of high industrial relevance due to its potential use in, for example, shock absorbers [13], drug delivery devices [14], and temperature-sensitive [15] and CO_2 sensors [16]. The prototype of a breathing MOF is the well-studied MIL-53(Al), consisting of 1D aluminum-oxide chains linked by benzenedicarboxylate (BDC) linkers [17]. Under the influence of external stimuli such as a mechanical pressure [13], temperature [18], and the adsorption and desorption of guest molecules [19], MIL-53(Al) can undergo a transition between a LP phase and a CP phase (see Figure 1).

Given the importance of the breathing behavior, the elucidation of the underlying mechanism in MIL-53(Al) has been the subject of research lately. Thermodynamic considerations have unraveled the macroscopic conditions governing breathing [12, 20]. At the microscopic level, it has been suggested that lattice vibrations trigger the observed flexibility, as the structural dynamics in MOFs strongly depends on their terahertz vibrations [21–24]. Liu et al. suggested that twisting motions of the phenyl rings induce the transformation from the CP to the LP phase at

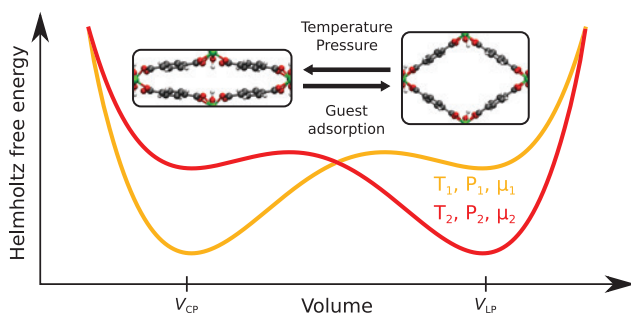


Fig. 1: Illustration of hypothetical Helmholtz free energy profiles of MIL-53(Al) as a function of the volume. The minima indicate the existence of a (meta)stable CP and LP phase, which are visually represented. A transition between both phases can occur under the influence of temperature, pressure, and/or the adsorption of guest molecules. For example, by increasing the temperature, MIL-53(Al) can undergo a transition from the CP phase to the LP phase [18].

high temperatures, since such twists are less restricted in the LP phase [18]. Furthermore, it has been shown that the CP phase is the most stable structure at low temperatures due to dispersion stabilization effects and that the larger vibrational entropy in the LP phase causes the CP-to-LP transition at high temperatures [15, 25]. We have recently proposed additional terahertz vibrations as driving forces for the breathing phenomenon [24]. Although our work provided a detailed picture of the vibrational fingerprints in both the CP and the LP phase separately, it remains an open question how the typical vibrations change in terms of the volume and which vibrations dominate the phase transformation.

Besides governing the structural dynamics of a material, lattice vibrations also contribute to the thermodynamic potential. This thermodynamic potential defines the (meta)stable states of the system and their relative stability (see Figure 1 for an illustration). Some of the present authors showed that the thermodynamic potential yields insight into the macroscopic conditions that affect breathing [12]. However, the impact of individual vibrations on the total thermodynamic potential has not been studied so far. Nevertheless, this would result in a better view on the circumstances giving rise to the breathing phenomenon.

Lattice vibrations can be studied by spectroscopic techniques, such as infrared (IR) and Raman spectroscopy, and inelastic neutron scattering, which enable to experimentally describe (part of) the material's vibrational fingerprints. However, under realistic experimental conditions, MIL-53(Al) shows no (meta)stable structures with a unit cell volume between those of the CP and LP phases in the absence of guests, which makes it impossible to track the evolution of lattice vibrations during the transition by means of such experimental techniques.

From a theoretical point of view, it is possible to perform simulations at intermediate volumes, which facilitates the connection of equivalent modes.

This work will fill the aforementioned gaps and provide a detailed understanding of the lattice vibrations of MIL-53(Al) and its influence on the thermodynamic properties of the material. For that purpose, the vibrational modes and their corresponding frequencies have been computed at several unit cell volumes via solid-state density-functional theory (DFT) calculations. This allowed us to determine the evolution of the IR spectrum of MIL-53(Al) as a function of the volume and to construct volume-frequency relations for each mode separately. In this way, the vibrational fingerprints in the CP and the LP phases of MIL-53(Al) could be linked unequivocally. The focus will be on the terahertz vibrations and their impact on the breathing transition. Furthermore, the quasi-harmonic approximation (QHA) [26, 27] has been applied, which enabled us to construct the Helmholtz free energy profile as a function of the volume at different temperatures. Finally, various mechanical and thermal thermodynamic properties such as the specific heat capacity, the bulk modulus, and the volumetric thermal expansion coefficient were derived from this profile and their dependence on specific terahertz vibrations is highlighted.

The remainder of this article is organized as follows. First, the computational settings of our calculations will be reported and the procedure used to construct the volume-frequency relations of the vibrational modes will be rationalized. Afterwards, the evolution of the normal mode vibrations as a function of the volume will be discussed. In the end, the influence of important terahertz vibrations on the thermodynamic properties of MIL-53(Al) will be examined.

Computational

Periodic simulations are performed with VASP [28] at the PBE-D3(BJ) level of theory [29–31] using a projector-augmented plane-wave basis set [32, 33] with a plane-wave cutoff of 600 eV. A $2 \times 6 \times 6$ Monkhorst-Pack k-mesh [34] is employed for structures with a unit cell volume smaller than 1200 \AA^3 , while a $2 \times 6 \times 2$ Monkhorst-Pack k-mesh is used for larger unit cell volumes [35]. The self-consistent field (SCF) cycle of an electronic structure calculation is terminated when the energy difference is lower than 10^{-8} eV. To construct the volume-frequency relations of MIL-53(Al), Hessians, i.e. the second-order derivatives of the energy with respect to the atomic coordinates, are determined at 26 unit cell volumes encompassing the

CP phase, the LP phase, and the transition region. Prior to each Hessian calculation, a fixed volume geometry optimization is performed, in which both the ions and cell shape are allowed to relax. The geometry optimizations are assumed to be converged when the energy difference between two subsequent steps decreases below 10^{-7} eV. The Hessians are calculated according to a finite difference scheme where the ions are displaced separately along the three directions with ± 0.01 Å. The vibrational modes are finally obtained by performing a normal mode analysis on the calculated Hessian with TAMkin [36].

To follow the evolution of the vibrational modes as a function of the volume, two different approaches are used. First, the IR spectrum of MIL-53(Al) is calculated at different volumes. Thereto, additional calculations of the Born effective charges are required at each unit cell volume, for which the density-functional perturbation theory method implemented in VASP is used [37, 38] similar to our previous study [24]. In addition to the volume-dependent IR spectrum, an alternative approach is used to investigate the volume dependence of vibrational modes. Based on a procedure applied by Erba et al. [26, 39], an explicit volume-frequency relation of each vibrational mode is constructed by evaluating the scalar products of this mode at a certain unit cell volume with all eigenmodes at the next unit cell volume. The vibrational mode is subsequently linked with the eigenmode yielding the highest scalar product (see Supporting Information Section S1). These volume-frequency relations can be constructed for all vibrational modes enabling the study of IR inactive vibrations.

After calculation of the electronic energies and the vibrational frequencies at distinct unit cell volumes, the thermodynamic and mechanical properties can be evaluated. The central quantity is the Helmholtz free energy F , which is the sum of the electronic energy E_{el} and a vibrational contribution F_{vib} ,

$$F(V, T) = E_{el}(V) + F_{vib}(V, T) \quad (1)$$

$$F_{vib}(V, T) = \frac{1}{2} \sum_{i=1}^N \hbar \omega_i(V) + k_B T \ln \left(1 - e^{-\frac{\hbar \omega_i(V)}{k_B T}} \right) \quad (2)$$

Here, \hbar and k_B represent the Planck and Boltzmann constant, respectively. $\omega_i(V)$ is the volume-frequency relation of mode i multiplied by 2π . At temperature $T = 0$ K, F_{vib} still contributes to the Helmholtz free energy via the zero-point energy (ZPE),

$$\text{ZPE} = \frac{1}{2} \sum_{i=1}^N \hbar \omega_i(V) \quad (3)$$

Also the vibrational free energy can be subdivided in two contributions, i.e. an energetic part E_{vib} and an entropic part $-TS$,

$$F_{vib}(V, T) = E_{vib}(V, T) - TS(V, T) \quad (4)$$

$$E_{vib}(V, T) = \sum_{i=1}^N \hbar \omega_i(V) \left(\frac{1}{2} + \frac{1}{e^{\frac{\hbar \omega_i(V)}{k_B T}} - 1} \right) \quad (5)$$

From the Helmholtz free energy as a function of the volume, the bulk modulus K can be calculated by taking its second-order derivative with respect to the volume multiplied by the volume,

$$K(V, T) = V \frac{\partial^2 F(V, T)}{\partial V^2} \quad (6)$$

Furthermore, the volumetric thermal expansion coefficients α_V of the (meta)stable phases of MIL-53(Al) can be computed from the Helmholtz free energy profile. First, the equilibrium volumes of these phases need to be identified as the minima of the Helmholtz free energy profile for different temperatures. Subsequently, α_V is calculated by taking the derivative of the equilibrium volume with respect to temperature,

$$\alpha_V(T) = \frac{1}{V(T)} \frac{\partial V(T)}{\partial T} \quad (7)$$

Finally, also the heat capacity at constant volume C_V and constant pressure C_p can be obtained starting from the volume-frequency relations and previously derived properties,

$$C_V(V, T) = \sum_{i=1}^N \frac{(\hbar \omega_i(V))^2}{k_B T^2} \frac{e^{\frac{\hbar \omega_i(V)}{k_B T}}}{\left(e^{\frac{\hbar \omega_i(V)}{k_B T}} - 1 \right)^2} \quad (8)$$

$$C_p(T) = C_V(T) + \alpha_V^2(T) K(T) V(T) T \quad (9)$$

Discussion

Following the procedures explained in Section “Computational”, the volume dependence of the vibrational fingerprints in MIL-53(Al) can be investigated. First, the volume dependence of the IR spectrum is examined. Several vibrational modes, showing large spectral changes over the calculated volume range, are discussed. Afterwards,

the volume-frequency relations of the terahertz vibrations within MIL-53(Al) and their possible role in the breathing mechanism are discussed. Once a clear picture of the lattice vibrations is obtained, some thermodynamic properties of MIL-53(Al), calculated within the QHA, are presented. Those results are compared with experimental and computational reference data and possible deviations are addressed, focusing on the influence of specific terahertz vibrations.

Lattice vibrations

In this subsection, the evolution of various vibrational frequencies is tracked as a function of the volume based on two techniques described in the computational details (see Section “Computational”). In the first approach, the IR spectrum is computed at different unit cell volumes, which only shows the changes of frequencies for IR active vibrations. The focus will be on the fingerprint vibrations that have been reported as ideal identifiers to detect the breathing transition [24, 40, 41]. Moreover, volume-frequency relations are constructed which allow to investigate all vibrational modes, including IR inactive ones. The volume-frequency relations will be used to detect terahertz vibrations with deviating behavior, as these are potential triggers for the breathing transition.

IR spectra

Experimentally, only the IR spectra of the (meta)stable CP and LP phases have been measured as an *in situ* measurement of the IR spectrum during the phase transformation is not yet possible. These experimental reports describe several IR active vibrations that distinguish the CP phase from the LP phase [24, 40, 41]. It is observed that the vibrational frequencies of most of these vibrations increase after transition from the CP to the LP phase and thus cost more energy. In our theoretical approach, it is possible to predict the volume-dependency of these IR fingerprints. The calculated IR spectrum of MIL-53(Al) as a function of the volume is represented in Figure 2a. The fingerprint vibrations are labeled in correspondence with our earlier work [24] (Labels from A to I, further explained in the caption of Figure 2). To facilitate the recognition of specific trends, the volume-frequency and volume-IR-intensity relations of these specific modes are represented in Figure 2b and c, respectively.

Starting with the IR intensities as a function of the volume (Figure 2c), no clear trend can be observed.

Moreover, the intensity difference between the vibrational modes in the CP and the LP phases is small, except for mode A1 (symmetric stretching of aluminum-oxide backbone), which doubles in intensity when going from the CP toward the LP phase.

A more interesting behavior is observed for the volume-frequency relations. The vibrational frequencies of the majority of the fingerprint vibrations follow a certain trend as a function of the volume. Three regimes can be distinguished (see Figure 2). In the first regime, at low unit cell volumes, the frequency strongly decreases as a function of the volume. A second regime starts around the volume where the CP phase is stable (843 Å³ from electronic structure calculations). From this point onwards, the vibrational frequencies of most normal modes steadily increase until the volume region of the stable LP phase is encountered (1426 Å³ from electronic structure calculations). Finally, the frequency drops again in the third regime at high unit cell volumes. The strong decrease in frequency as a function of the volume in regimes 1 and 3 can be explained by the weakening of covalent interactions. This can be illustrated by looking at the example of the aluminum-oxide bond (Figure 3a–c). At very low and high volumes, the bond distance strongly increases as a function of the volume indicating a decrease in the strength of the covalent bond. At the same time, the frequencies of all stretching vibrations of the aluminum-oxide bond decrease (the corresponding frequency region is highlighted by a gray background in Figure 2a). Within regime 2 the strength of the covalent interactions remains more or less unaltered as the bond distances remain almost constant. Nevertheless, an increase in the vibrational frequency is observed as a function of the volume. This is a result of dispersion interactions, which are important in MIL-53(Al) [15] (see Supporting Information Section S2).

Some modes differ from the general volume-frequency trend, for example the wagging mode of the CH-bonds (mode B in Figure 2), the antisymmetric stretching mode of the carboxyl group (mode I in Figure 2), and the bend and stretch modes of the hydroxyl group around 970 cm⁻¹ (D in Figure 2) and 3750 cm⁻¹ (Figure 3e), respectively. Limiting the discussion to the last two examples, it is observed that the hydroxyl bend vibration shows a decreasing frequency for increasing volumes at small unit cell volumes and afterwards the frequency increases, but instead of going down again it keeps on increasing. The hydroxyl stretch vibration shows the opposite behavior: at small volumes, the frequency increases upon increasing volume, but it starts decreasing at larger volumes. Those modes are extremely localized, which makes them only dependent on the geometry of the hydroxyl group.

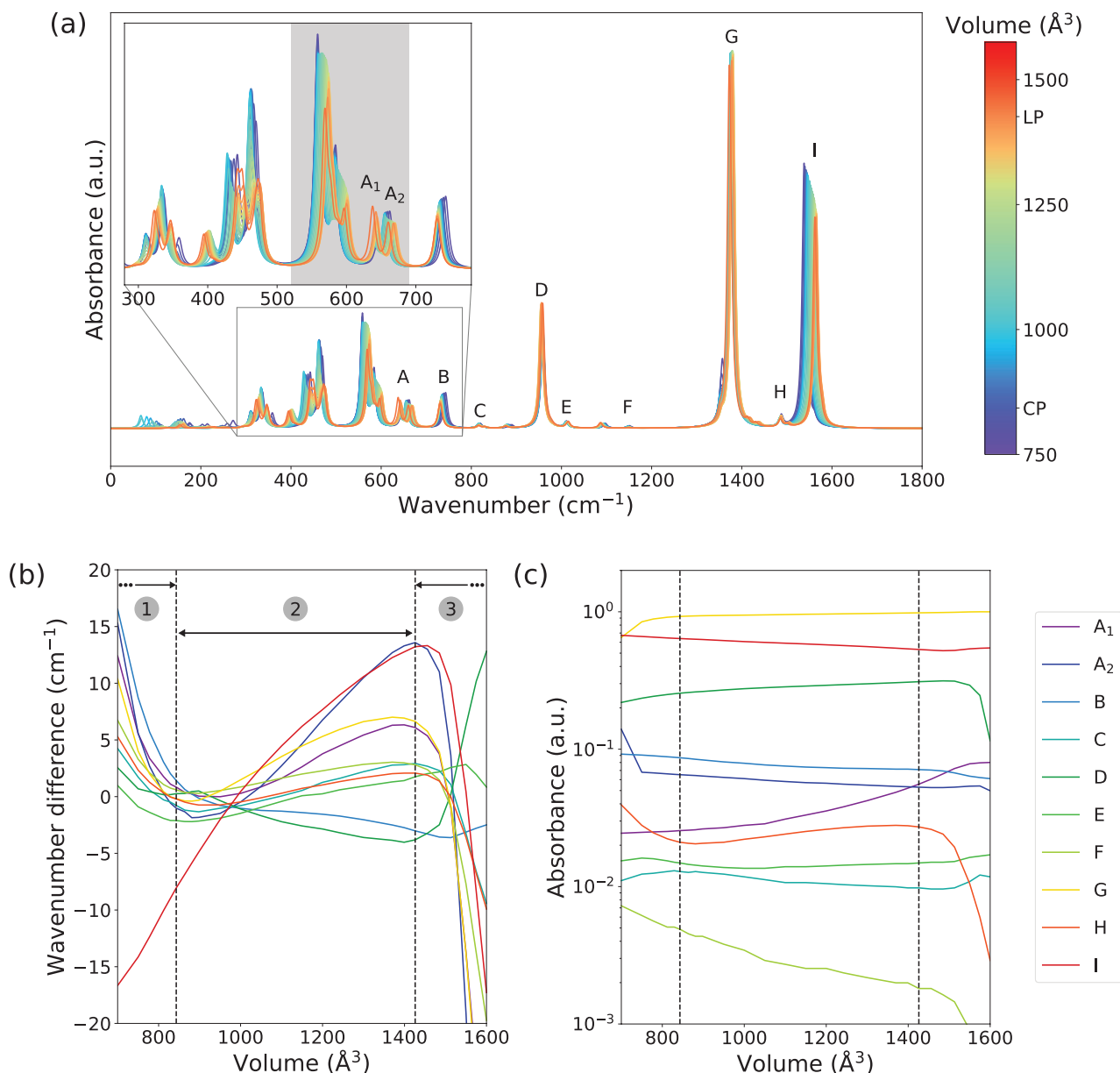


Fig. 2: (a) Theoretical IR spectra of MIL-53 (AI) at different unit cell volumes within the wavenumber range 0–1800 cm^{-1} . The inset zooms in upon the range 280–780 cm^{-1} . The region of the aluminum-oxide stretch vibrations is highlighted with a gray background. Fingerprint vibrations, identified in earlier reports [24, 40, 41], are indicated with a capital letter and follow the same labeling as in Ref. [24]. (A1) Symmetric stretching of the aluminum-oxide backbone. (A2) Antisymmetric stretching of the aluminum-oxide backbone. (B) Out-of-plane wagging of hydrogen atoms on the aromatic ring. (C) Bending of the carboxyl group and within the aromatic ring. (D) Rocking of hydroxyl group. (E) Bending within the aromatic ring. (F) Stretching between the aromatic ring and the carboxyl group. (G) Symmetric stretching of the carboxyl group. (H) Stretching between the aromatic ring and the carboxyl group. (I) Antisymmetric stretching of the carboxyl group. (b) Volume-frequency relations of the IR fingerprint vibrations. The wavenumbers are shifted by their average value over the computed volume range. Dotted lines indicate the equilibrium volumes of the CP and LP phases obtained from electronic structure calculations. The volume ranges of the three different volume-frequency regimes are indicated. (c) Volume-IR-intensity relations of the IR fingerprint vibrations. Dotted lines indicate the equilibrium volumes of the CP and LP phases obtained from electronic structure calculations.

Looking at the volume-frequency relations of the hydroxyl stretch vibrations and the bond length of the hydroxyl group as a function of the volume (Figure 3e and f, respectively), there exists indeed a clear correlation between the

bond length and the vibrational frequency of the hydroxyl group.

For wavenumbers between 300 and 500 cm^{-1} , the IR spectrum as a function of the volume shows more abrupt

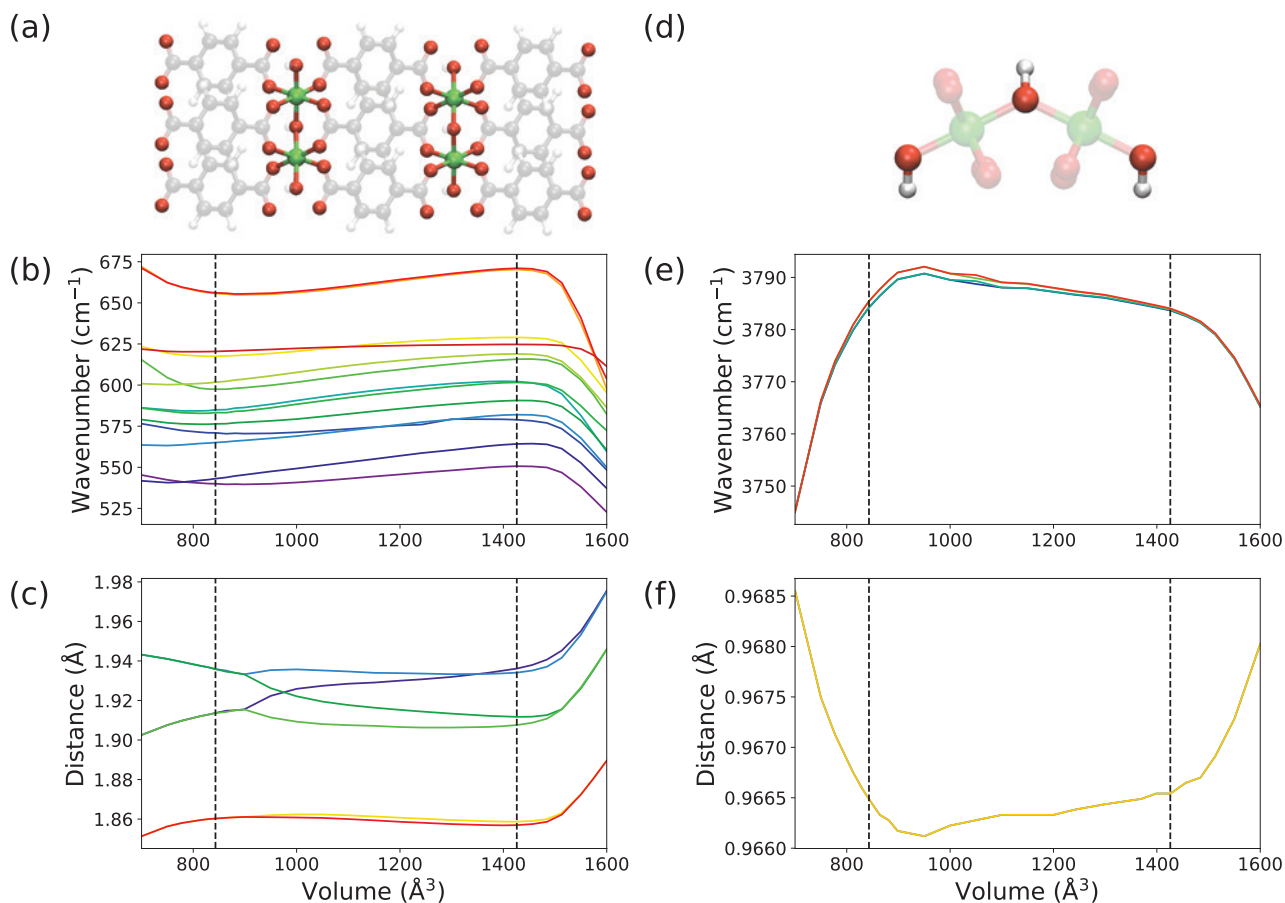


Fig. 3: (a) Visualization of the aluminum-oxide bonds. (b) Volume-frequency relations of all vibrational modes describing stretches of aluminum-oxide bonds. (c) Length of the aluminum-oxide bonds as a function of the volume. (d) Visualization of the hydroxyl bond. (e) Volume-frequency relations of all hydroxyl stretch vibrations. (f) Length of the hydroxyl bond. Dotted lines indicate the equilibrium volumes of the CP and LP phases obtained from electronic structure calculations.

changes. This is caused by a change in IR activity of specific modes, rather than deviations from the general volume-frequency trend (see Supporting Information Section S3). In our previous work [24], it was argued that some of the changes in IR activity originate from rocking of the hydroxyl group, which is present at large volumes, but suppressed at small volumes. This claim is confirmed in our simulations.

Terahertz vibrations

The terahertz region ($<300\text{ cm}^{-1}$) is especially interesting for soft porous crystals as it contains the modes which influence the dynamics of the framework most profoundly. In this frequency region, the IR spectrum of MIL-53(Al) contains only a few IR active modes, so we have to restrict our discussion to the volume-frequency relations to obtain a complete view of the vibrational spectrum (Figure 4). It is clear that the behavior of low-frequency modes differs

from the behavior of high-frequency modes as it concerns mainly collective vibrations. Here, the modes showing the most interesting volume-frequency curves are highlighted. First of all, the vibrations describing linker rotations (indicated in blue in Figure 4) and trampoline-like motions (red curves in Figure 4) are discussed. Similar terahertz vibrations were recently reported around the same frequencies in MIL-140A, a Zr-based MOF with BDC linkers [42]. We find in our study that such modes display a large increase in frequency for decreasing unit cell volume, as these vibrations are heavily constrained at small unit cell volumes. Among the vibrations exhibiting linker rotations, two types can be distinguished, which do also appear in the MIL-140A framework [42]. Namely, those where opposite linkers rotate in the same direction and those where opposite linkers rotate in the opposite direction. The former are heavily constrained in dense structures yielding high vibrational frequencies, while the latter are less restricted in small unit cells. This causes a splitting of their volume-frequency relations

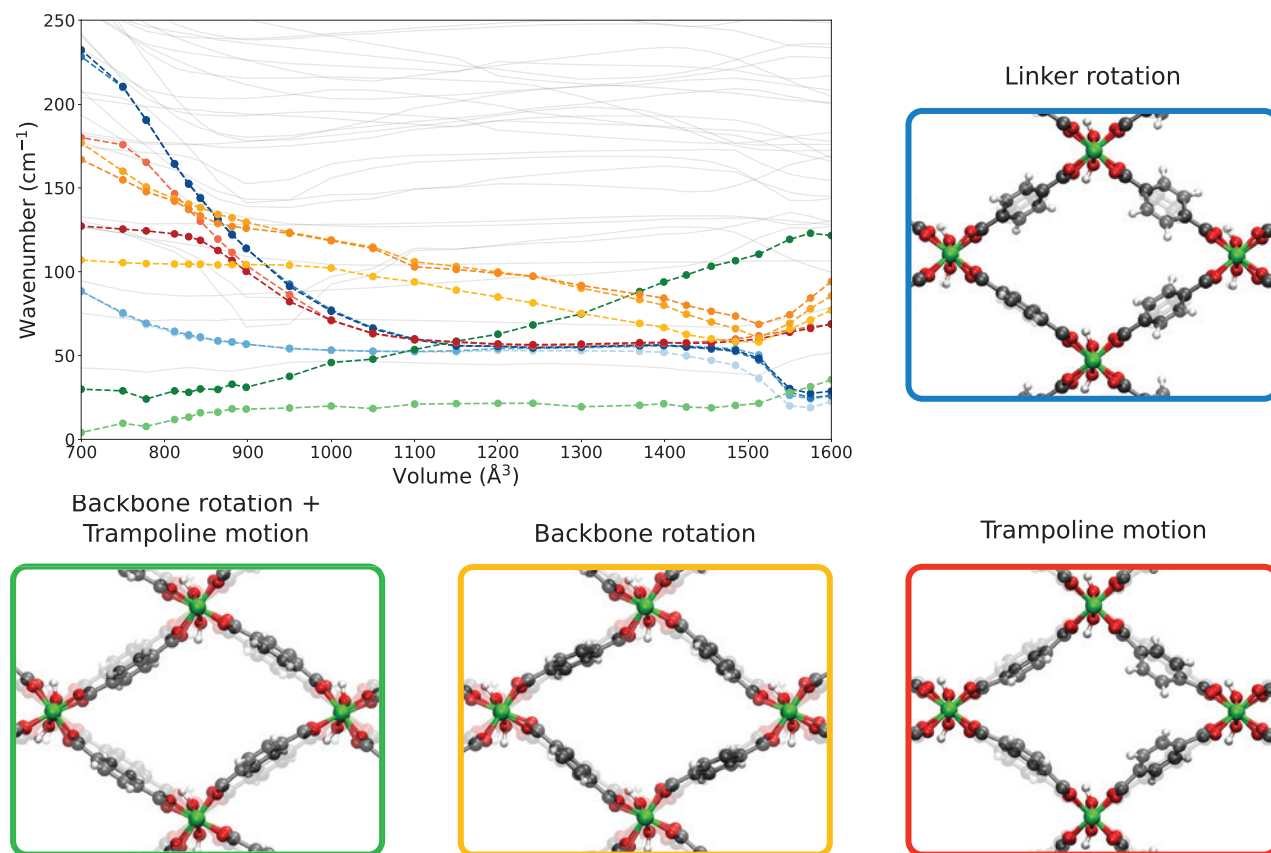


Fig. 4: Volume-frequency relations of the terahertz vibrations in MIL-53(Al). The collective vibrations with the most significant frequency differences over the computed volume range are highlighted and visually represented. Blue curves: vibrations inducing linker rotations. Green curves: soft modes combining translations and rotations of the aluminum-oxide backbone and the linkers. Yellow curves: vibrations inducing rotations of the aluminum-oxide backbone. Red curves: trampoline-like vibrations.

around 1200 \AA^3 . It has to be noted that, according to our simulations, the vibrational frequencies of all linker rotation modes show a sudden decrease when increasing the volume above 1520 \AA^3 . This decrease in frequency is induced by a decrease in the dihedral angles of the Al-O-C-O units, illustrated in Figure 5. For large volumes this dihedral angle approaches zero, which lowers the energy barrier for linker rotations and thus its corresponding vibrational frequency. This sudden decrease in frequency results in a large increase of the vibrational entropy (see Section “Thermodynamic properties”) which may trigger the CP-to-LP phase transformation.

Furthermore, there are three modes showing rotations of the metal-oxide backbone (yellow curves in Figure 4). This rotation is also constrained at small volumes, hence the increase in frequency upon lowering the volume, but the frequency also increases at large volumes. This probably results from linkers which become overstretched when the backbone rotates at large volumes. Finally, two modes have a completely different volume-frequency relation, showing a continuous increase in frequency upon

increasing volume (green curves in Figure 4). Both modes consist of a combination of linker and metal-oxide chain movements. The mode that has the lowest frequency over the entire volume range can be described by a rotation of the metal-oxide backbones, which induces a trampoline-like motion of the linkers (see green box in Figure 4 for a visualization). The other mode shows a translation of the metal-oxide backbones, inducing a rotation of the linkers (see Supporting Information Section S4 for a visualization). The volume-frequency relations of these two modes are strongly coupled with the volume-dependency of the diagonal elements of the Lagrangian strain tensor η [43] (see Figure 6). The latter can be obtained by taking matrix products of the cell matrices at a reference unit cell volume, \mathbf{h}_0 , and a deformed unit cell volume, $\mathbf{h}(V)$:

$$\eta(V) = \frac{1}{2}(\mathbf{h}_0^{-T} \mathbf{h}^T(V) \mathbf{h}(V) \mathbf{h}_0^{-1} - \mathbf{1}) \quad (10)$$

The vibrational frequency as a function of the volume of the mode exhibiting rotations of the aluminum-oxide

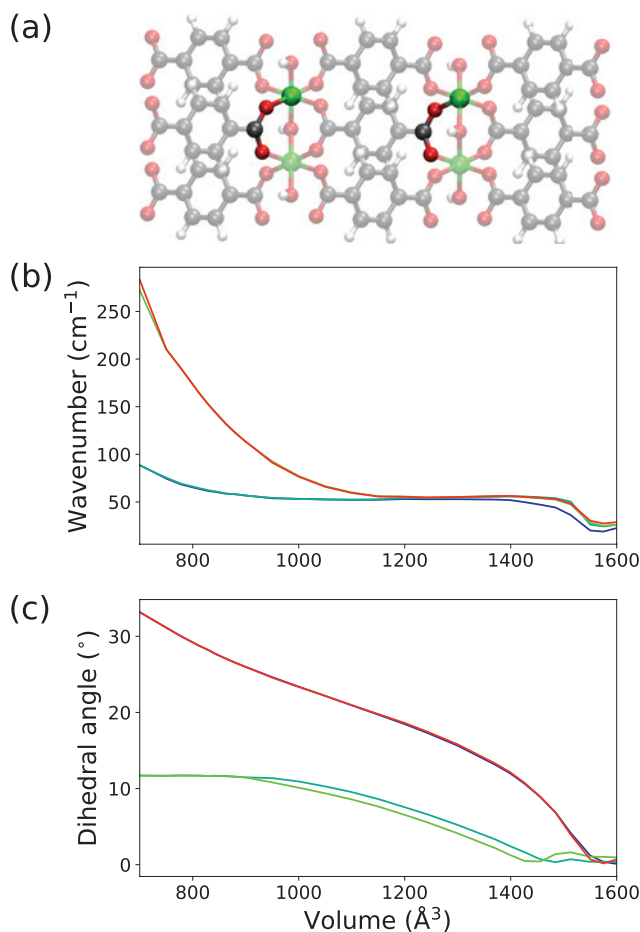


Fig. 5: (a) Visualization of the Al-O-C-O dihedral. (b) Volume-frequency relations of the terahertz vibrations exhibiting rotations of the linkers. (c) Different Al-O-C-O dihedrals.

chain is strongly linearly correlated with the strain along this chain, η_{xx} , as a function of the volume. Moreover, a linear relation is observed between the volume-dependency of the vibrational frequency of the mode characterized by translations of the aluminum-oxide backbone and the strain along the pore diagonals, η_{yy} and η_{zz} , as a function of the volume. This correspondence indicates that the particular volume-frequency relations of these two terahertz vibrations originate from the strain developed within the framework. As such, this procedure allows us to reveal the relevant vibrational modes that are most affected by the breathing-induced strain in the material, a macroscopic property, through the strain tensor. As both modes become very soft at small volumes, they are very important for the dynamics in the CP phase of MIL-53(Al). The vibration inducing rotations of the aluminum-oxide backbone, for example, can trigger the transition from a closed pore phase to a very closed pore phase as reported in MIL-53(Sc) [44]. In the remainder, we will refer to these two modes as soft modes.

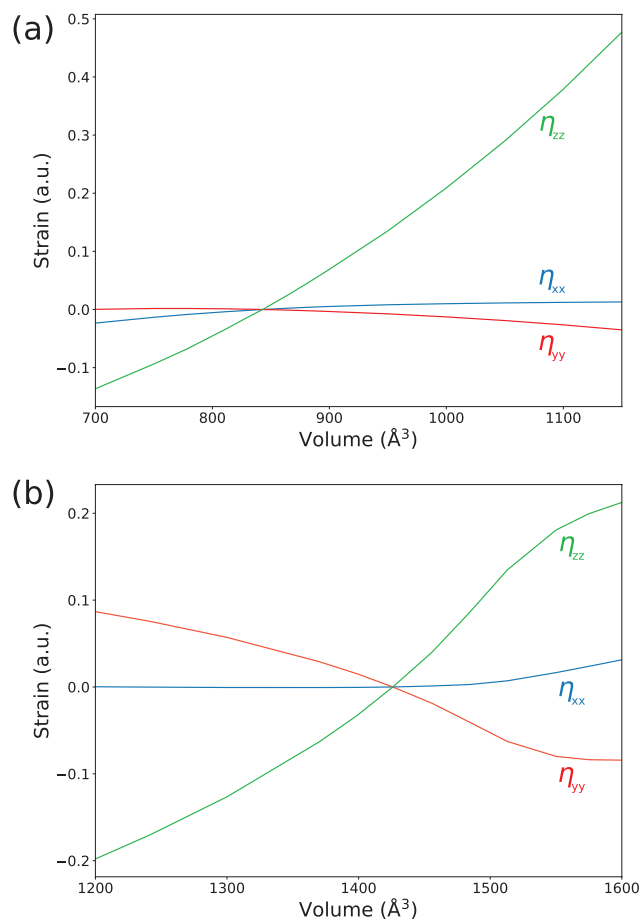


Fig. 6: The strain within MIL-53(Al) along the three Cartesian directions as a function of the volume for structures with the CP phase (843 Å³) as reference volume (a) and the LP phase (1426 Å³) as reference volume (b). The volume-dependency of the strain along the aluminum-oxide chain, η_{xx} , is small and proportional to the volume-frequency relation of the soft mode exhibiting rotations of the metal-oxide backbone. The volume-dependency of the strains along the pore diagonals, η_{yy} and η_{zz} , is large and proportional to the volume-frequency relation of the soft mode exhibiting translations of the metal-oxide backbone.

Thermodynamic properties

Up to this point, the direct influence of vibrational modes on the lattice dynamics was investigated. However, normal mode vibrations also contribute to the thermodynamic potential, which in its turn can teach us more about the macroscopic conditions that govern breathing [12]. In this section, this thermodynamic potential will be examined by looking at several mechanical and thermal thermodynamic properties of MIL-53(Al), which can be approximated from the vibrational frequencies at different unit cell volumes obtained by our calculations. First of all, the Helmholtz free energy profile will be constructed and afterwards some derived properties will be determined.

As vibrational modes at different unit cell volumes were successfully matched in the previous section, it becomes possible to assess the influence of specific modes to the thermodynamic quantities.

Helmholtz free energy profile

Starting from the analytic expressions for the volume-frequency relations, obtained after fitting a ninth-order Taylor expansion to the data points, the Helmholtz free energy profile as a function of the volume can be constructed at different temperatures (Figure 7a). Those results are compared with the electronic energy profile without vibrational contributions such as the zero-point energy (ZPE) (black curve).

Within the considered temperature window, we recognize two minima in the Helmholtz free energy profile corresponding to the presence of the (meta)stable CP and LP phases. At 1 K, the equilibrium volumes of the CP and the LP phases are located around 860 and 1461 Å³, respectively. Using another degree for the fitted polynomials can shift these values by 5 Å³, introducing an uncertainty on the predicted values. Note that, even at 1 K, the Helmholtz free energy profile differs substantially from the electronic energy profile. The main effect of the ZPE is a shift of the equilibrium volumes of both the CP and LP phases by about 20 Å³. The value for the CP phase volume corresponds well with the experimental value measured by Liu et al. [18] at 77 K, while the LP phase volume is slightly overestimated in our simulations. The free energy difference between the (meta)stable phases is nearly unaffected by the ZPE and has a value of 26 kJ · mol⁻¹ at 1 K. This free

energy difference falls in the range of the results obtained by other computational studies [15, 25, 45].

By looking at the temperature response of the Helmholtz free energy profile, a slight increase in equilibrium volumes is observed for both the CP and the LP phases for temperatures above 50 K. More pronounced is the decrease of the free energy difference for increasing temperatures. It reaches values of 19 and 14 kJ · mol⁻¹ at 300 and 500 K, respectively. This behavior is expected as the LP phase is entropically favored over the CP phase [15, 18, 25]. However, even for temperatures as high as 500 K, the LP phase has not become the most stable phase, while the experimental CP-to-LP transition temperature is found around 350 K [18]. This deviation with the experimental observations is caused by an exaggerated stability of the CP phase due to the applied computational methodology [15]. The PBE-D3(BJ) level of theory, used in this work, overestimates the dispersion interactions, which results in an unphysical stabilization of the CP phase. This point was extensively studied in a recent contribution by some of the presenting authors [15]. When the random-phase approximation is applied, a higher level of theory for a more accurate description of correlation effects, the electronic energy difference between the CP and the LP phase reduces to about 7 kJ · mol⁻¹ [15]. Given the excessive computational cost and the current computational resources, a vibrational analysis using the latter approach is not feasible. Nevertheless, starting from the energy difference at the RPA level of theory and considering the vibrational frequencies as predicted in this work using PBE-D3(BJ), the CP and LP phases become equally stable around 300 K (see Supporting Information Section S5), which is more in line with experimental observations [18]. Furthermore,

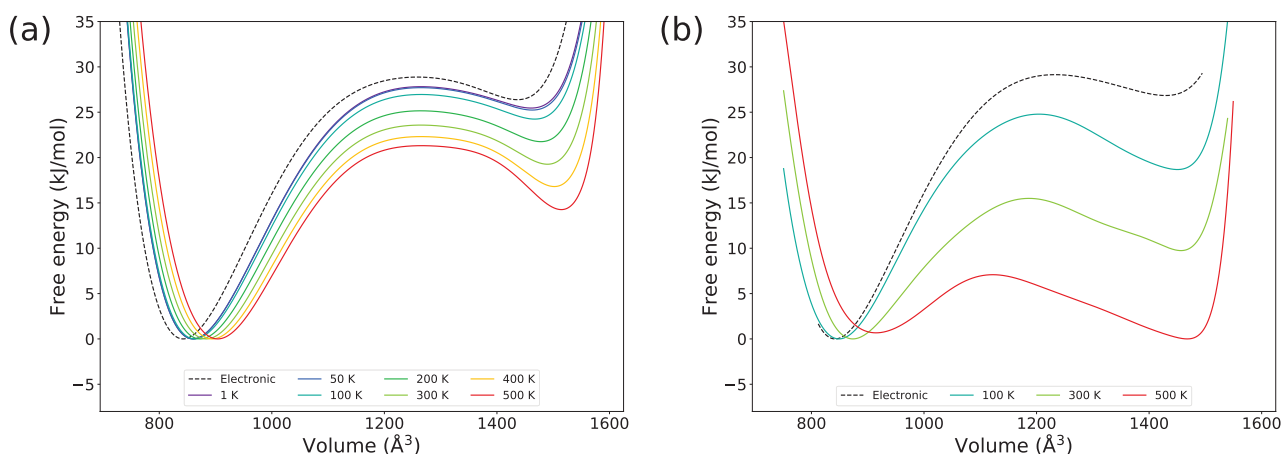


Fig. 7: Helmholtz free energy as a function of the volume at different temperatures (solid lines) and the electronic energy as a function of the volume (black dashed line) using the QHA (a) (this work) and dynamic methods (b) (Figure reproduced from Ref. [45] with permission of the American Chemical Society).

comparison of the lattice vibrations at the PBE-D3(BJ) level of theory with a hybrid functional did not yield significant changes (see Supporting Information Section S5). Finally, in our earlier study a good agreement was found between the experimental IR and Raman spectra and the computational spectra at the PBE-D3(BJ) level of theory [24]. This hints at a reliable prediction of the lattice dynamics at the current level of theory. To conclude this paragraph, it is worth mentioning that the Helmholtz free energy profile in Figure 7a is constructed via the QHA, which still neglects certain anharmonic effects. By including these effects via dynamical methods, which are computationally more expensive, an increased entropic stabilization of the LP phase is observed [45] (see Figure 7b). Although, it has to be noted that the results obtained from these ab initio molecular dynamics simulations are prone to large sampling uncertainties.

Energetic and entropic contributions

The specific temperature dependence of the Helmholtz free energy profile can be more thoroughly understood when considering the contributions of the electronic energy, the vibrational energy and the entropy to the free energy. The free energy difference between the LP and the CP phases of these contributions and the total free energy difference as a function of temperature are presented in Figure 8. At low temperatures, the total free

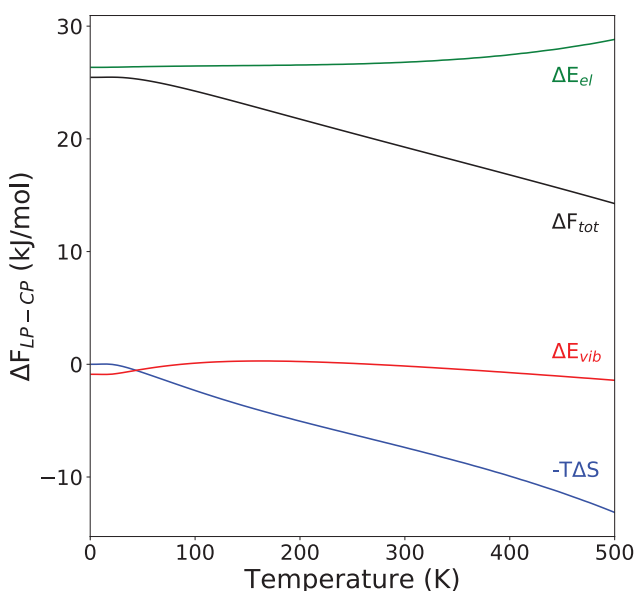


Fig. 8: Total free energy difference between the LP and CP phases as a function of temperature, ΔF_{tot} (black curve), and its three contributions: entropy $-T\Delta S$ (blue), vibrational energy ΔE_{vib} (red), and electronic energy ΔE_{el} (green).

energy difference between the LP and the CP phases is mainly the result of the difference in electronic energy. Furthermore, this plot illustrates that the difference in the vibrational energy between the LP and the CP phases is limited over the complete temperature range, whereas the difference in entropic contribution decreases significantly, canceling out the increase in the electronic energy difference. As temperature alters the equilibrium LP and CP volumes, also the electronic energy difference between these two phases will change even though the electronic energy in itself is temperature independent at a fixed volume. The steady decrease in the difference of the entropic contribution originates from the activation of the vibrations inducing linker rotations, which have very low frequencies at large unit cell volumes. As a consequence, the entropic stabilization of the LP phase is mainly the result of this type of vibrations, as already suggested by Liu et al. [18].

Contributions from vibrational modes

Up to this point, we could identify the vibrations exhibiting linker rotations as important contributors to the Helmholtz free energy profile, but they are not the only ones shaping the free energy landscape. This becomes clear when analyzing the vibrational free energy profile of each mode separately (Figure 9). At 1 K, the vibrational free energy is restricted to the ZPE. Several terahertz modes undergo a large frequency change as a function of the volume and, therefore, they yield ZPE differences over the calculated volume range as large as $1.2 \text{ kJ} \cdot \text{mol}^{-1}$. Nonetheless, their impact on the total free energy profile remains small as also multiple localized vibrations give rise to a substantial ZPE difference. At 300 K, the picture looks completely different. Now, the vibrational free energy differences are dominated by the terahertz vibrations. First in line are the vibrations exposing linker rotations (blue curves) which generate free energy differences of at least $4 \text{ kJ} \cdot \text{mol}^{-1}$, favoring open pore structures. However, these modes are counteracted by the soft modes (green curves), showing combined collective behavior of the linkers and the metal-oxide backbones. The magnitude of the free energy difference produced by these two vibrations are of comparable size to the free energy difference of the vibrations exhibiting linker rotations. As such, it can be expected that these modes are of crucial importance in the LP-to-CP phase transition at low temperatures and that they partially hinder the transition from the CP to the LP phase at elevated temperatures. Other modes worth mentioning are those inducing trampoline-like motions of the linkers (red curves) and metal-oxide backbone rotations

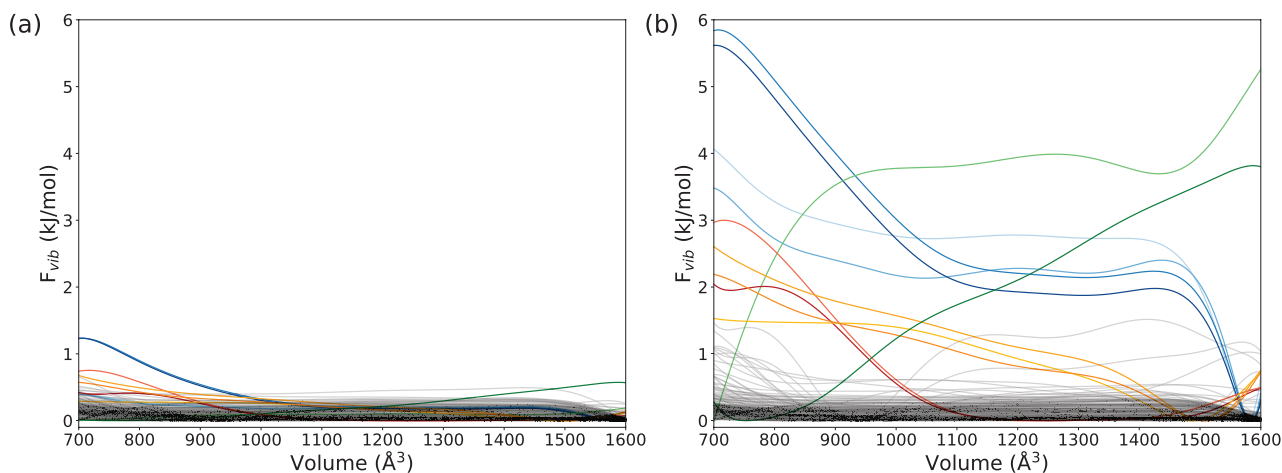


Fig. 9: Contributions of the different vibrational modes to the Helmholtz free energy at 1 K (a) and 300 K (b). The terahertz vibrations discussed in Section “Terahertz vibrations” are highlighted with the same colors as in Figure 4.

(yellow curves). These modes attribute considerably to the stabilization of the LP phase at high temperatures.

Derived properties

Besides the Helmholtz free energy profile, knowledge of the vibrational modes allows to predict other thermodynamic properties, such as the specific heat capacity, the bulk modulus, and the volumetric thermal expansion coefficient. The temperature dependence of these properties will be investigated in this subsection for both the CP and the LP phases. For a discussion of the pressure-versus-volume ($P(V)$) equation of state, we refer to the Supporting Information Section S6. As the bulk modulus and the volumetric thermal expansion coefficient are derived from the Helmholtz free energy profile, uncertainties on the latter due to fitting may accumulate. Therefore, the predicted values, obtained by fitting the Rose-Vinet equation of state [46] to the Helmholtz free energy profiles around the equilibrium volumes, will be presented together with an uncertainty region determined by the fitting of different orders of Taylor expansions to the volume-frequency relations.

Specific heat capacity

The specific heat capacity is a measure for the ability of a material to store heat. A large specific heat capacity will allow the material to absorb more heat and, as a consequence, increase its resistance against undesired thermal effects. The specific heat capacity at constant pressure for both the CP and LP phases are shown in Figure 10a in the temperature range 0–500 K. The curves of the

(meta)stable phases coincide almost over the complete temperature range, except for very low temperatures. In that region, the CP phase has a somewhat lower value as the heat capacity is dominated by the lowest vibrational frequency. The specific heat capacity increases monotonically with temperature from $0 \text{ Jg}^{-1}\text{K}^{-1}$ at 0 K towards $1.4 \text{ Jg}^{-1}\text{K}^{-1}$ at 500 K. These values remain unaffected by applying different fitting polynomials. Our predictions overestimate the experimental value obtained by Kloutse et al. only by $0.1 \text{ Jg}^{-1}\text{K}^{-1}$ [47].

Bulk modulus

The bulk modulus provides information on the resistance to isotropically compress a material. Therefore, this property is relevant in the study of the highly flexible MIL-53(Al) material. The bulk modulus is proportional to the second-order derivative of the Helmholtz free energy with respect to the volume. As a consequence, possible noise on the free energy due to fitting can yield large uncertainties in the predicted value of the bulk modulus. This is clearly visible in Figure 10b, where the predicted values, using different orders of polynomials, are represented by shaded areas. From the Rose-Vinet fit a value of 3.8 GPa is expected for the CP phase at 0 K, which reduces to 3.4 GPa at 300 K. This falls in the range of the results obtained by force field MD simulations at 300 K, which yield values between 3.3 and 3.7 GPa [49]. However, the bulk modulus at 0 K deviates substantially from the RPA result of 2.6 GPa [15]. In the latter, the ZPE was not taken into account, but our simulations suggest a decrease in bulk modulus when ZPE is included. The bulk modulus from the Rose-Vinet fit to the LP phase ranges from 2.1 GPa at 0 K to 8.4 GPa at 500 K. At 300 K, a value of 4.2 GPa

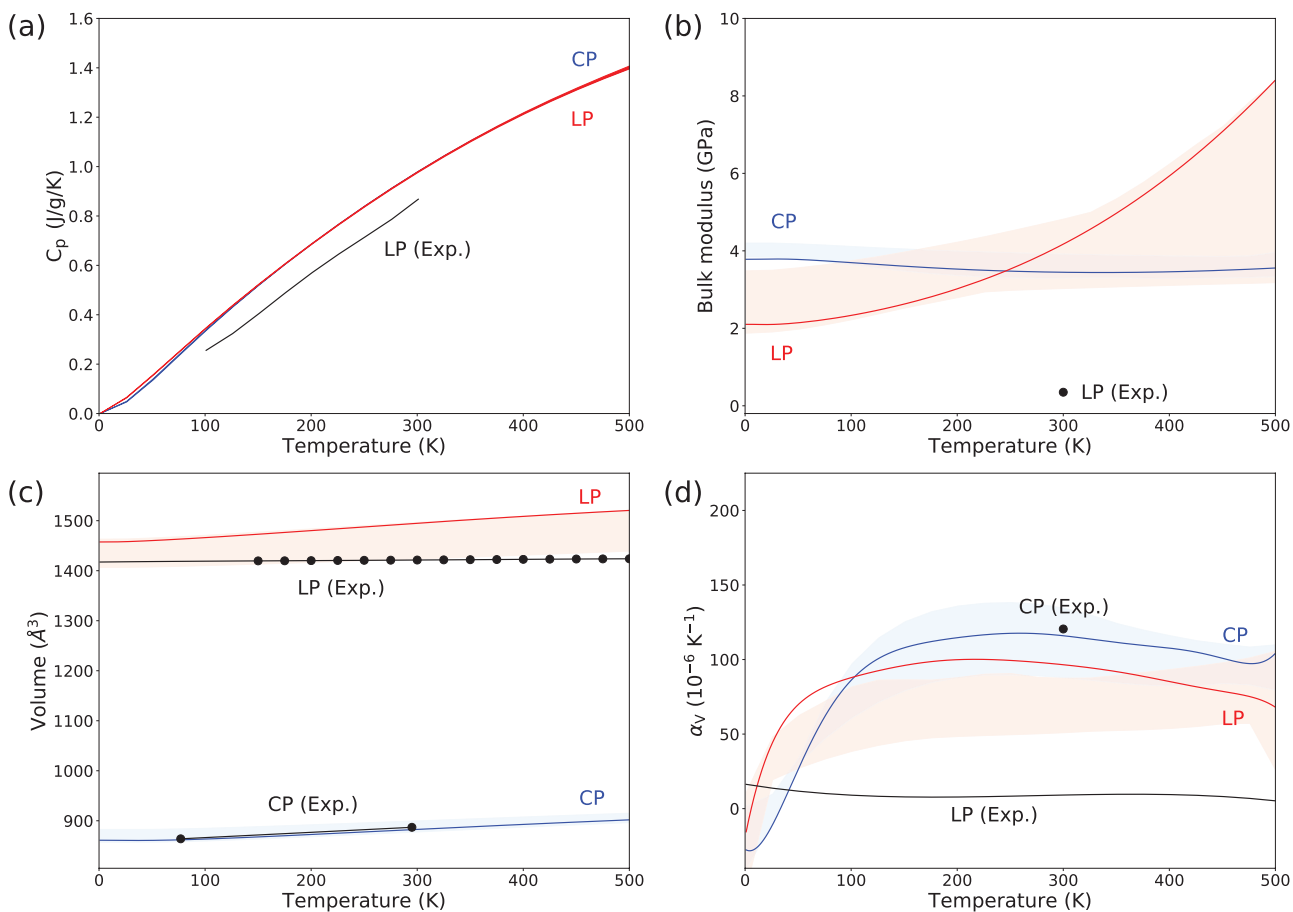


Fig. 10: Thermodynamic properties of the CP (blue) and LP (red) phases as a function of temperature. The blue and red solid lines represent the results from a Rose-Vinet fit [46] (except for the specific heat capacity). The shaded area represents the uncertainty due to the used fitting polynomial. (a) Specific heat capacity at constant pressure. (b) Bulk modulus. (c) Equilibrium volume. (d) Volumetric thermal expansion coefficient. All calculated properties are compared with experimental reference data from Refs. [13, 18, 47, 48].

is predicted, which overestimates the experimentally obtained result of 0.35 GPa by one order of magnitude [13] and also force field MD simulations give lower values [49]. In our simulations, the bulk modulus at 300 K is higher for the LP phase than for the CP phase, which is counterintuitive. The strong increase in the LP phase bulk modulus for increasing temperatures is a consequence of a too large volumetric thermal expansion (see next subsection). This shifts the equilibrium volume to regions where the electronic energy profile has a strong curvature.

Volumetric thermal expansion

A last thermodynamic property of MIL-53(Al) that can be obtained within the QHA is the volumetric thermal expansion coefficient. In order to derive this quantity for the CP and the LP phases, the equilibrium volumes have to be determined from the Helmholtz free energy profile within the temperature range of interest (Figure 10c). For the

equilibrium volume of the CP phase, we observe an excellent agreement with the experimental result [18], while the one of the LP phase [48] is consistently overestimated by our calculations.

The volumetric thermal expansion coefficient is proportional to the derivative of the equilibrium volume with respect to temperature. In Figure 10d, this thermodynamic quantity is presented. A large spread on the predicted value is noticed. Nonetheless, it can be concluded that the thermal expansion of the CP phase is lower than the one of the LP phase below 100 K, while the opposite holds for higher temperatures. Based on our simulations, we expect small negative thermal expansion (NTE) below 40 K for the CP phase, which turns into positive thermal expansion (PTE) at higher temperatures. This is also supported by the mode Grüneisen parameters, which often form an indication for NTE or PTE behavior [50] (see Supporting Information Section S7). The magnitude of the experimentally measured volumetric thermal expansion coefficient

of the CP phase at 300 K is $120 \cdot 10^{-6} \text{ K}^{-1}$, which is obtained by considering the equilibrium volumes at only two different temperatures [18]. Ab initio MD simulations (AIMD) predict values of the order $180 \cdot 10^{-6} \text{ K}^{-1}$ [45]. In contrast,

the thermal expansion coefficient of the LP phase overestimates the experimental result by one order of magnitude [48]. AIMD simulations give also a lower value for this property. The predicted value for the thermal expansion

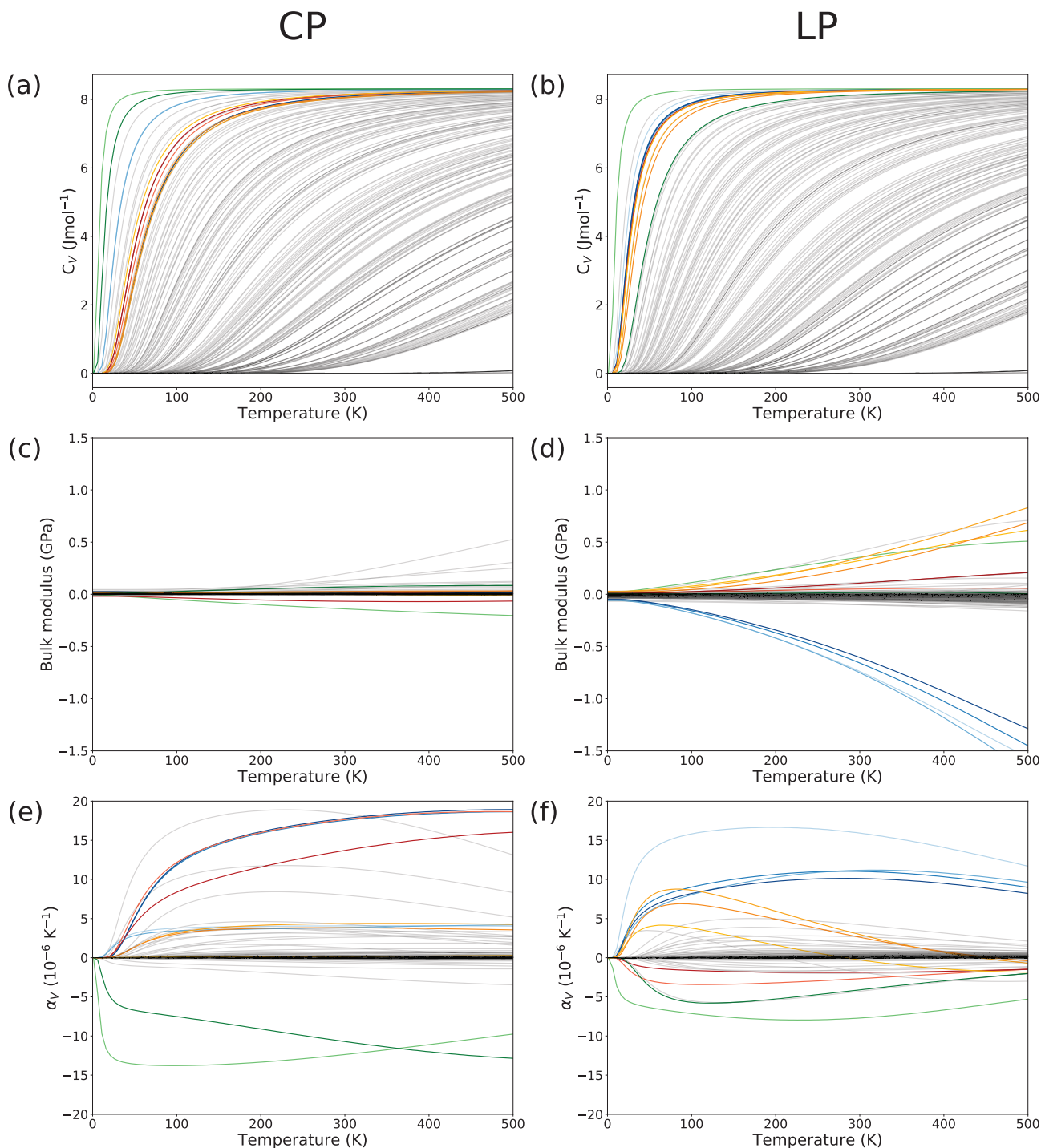


Fig. 11: Contribution of the lattice vibrations to the thermodynamic properties of the CP and LP phases as a function of temperature. The terahertz vibrations discussed in Section “Terahertz vibrations” are highlighted in the same color as in Figure 4. Heat capacity at constant volume of the CP phase (a) and the LP phase (b). Bulk modulus of the CP phase (c) and the LP phase (d). Volumetric thermal expansion coefficient of the CP phase (e) and the LP phase (f).

coefficient in the LP phase is heavily influenced by the linker rotation vibrational frequencies (see Section “Influence of lattice vibrations on thermodynamic properties”). Their entropic contribution to the Helmholtz free energy profile is peaked around 1570 \AA^3 , which can induce a relatively large shift in equilibrium volume at elevated temperatures.

Influence of lattice vibrations on thermodynamic properties

In previous paragraphs, we have argued that the thermodynamic properties are mainly affected by terahertz vibrations. As we have derived analytical expressions for the vibrational frequencies as a function of the volume, it becomes possible to determine the influence of each lattice vibration on the thermodynamic properties (see Supporting Information Section S8). In Figure 11, the vibrational contributions to the specific heat capacity at constant volume, the bulk modulus, and the volumetric expansion coefficient of the CP and LP phases are presented. Starting with the heat capacity at constant volume, we observe only minor differences between both phases. As the LP phase consists of more vibrations with very-low frequencies, it has a slightly larger total heat capacity at low temperatures, but once the contribution from these modes to the heat capacity is saturated, the total heat capacities of both phases have equal magnitudes.

The lattice vibrations have a more pronounced effect on the bulk modulus and the volumetric thermal expansion. The bulk modulus of the CP phase depends mainly on the contributions from the soft modes (green curves) and a few other low-frequency vibrations, although their magnitudes remain small below 500 K. For the LP phase structure, we observe a large negative contribution to the bulk modulus from the vibrations exhibiting linker rotations (blue curves) on the one hand and a large positive contribution from the vibrations describing rotations of the aluminum-oxide backbone (yellow) and one of the soft modes (green). The magnitudes of these contributions increase with temperature reaching values of -0.7 GPa and 0.4 GPa , respectively. The large negative bulk modulus of the vibrations inducing linker rotations has a considerable impact on the total bulk modulus. Nevertheless, the latter increases for increasing temperatures. This is a result of the curvature of the electronic contribution to the Helmholtz free energy profile, which increases for increasing equilibrium temperatures, as the equilibrium volume alters.

Finally, we discuss the mode contributions to the volumetric thermal expansion. For the CP phase, we notice

that the two soft modes (green) give a large negative contributions to the volumetric thermal expansion coefficient giving rise to NTE even at very low temperatures. At higher temperatures, there are more vibrational modes with a positive contribution to α_v , for example the vibrations inducing linker rotations (blue) and trampoline motions (red), yielding PTE. Also for the LP phase, the soft modes tend to lower the value of α_v , but they are counteracted by both the vibrations showing rotations of the linker (blue) and the metal-oxide backbone (yellow). Especially the modes with linker rotations have a large impact on the PTE behavior over the complete temperature range. We assume that an overestimation of the contribution of these low-frequency vibrations are the main cause of the too large α_v of the LP phase and, hence, the too large increase in equilibrium volume leading to an overestimation of the bulk modulus.

It is clear that terahertz vibrations have a considerable effect on the prediction of thermodynamic properties. Therefore, it is essential to simulate the vibrational frequencies of terahertz modes accurately, as small changes in the frequencies or their derivatives with respect to the volume can substantially affect the predicted thermodynamic properties. Although, even with high computational standards, a correct prediction of low-frequency vibrations remains hard when the potential energy surface is flat and/or anharmonicities are present [51, 52].

Conclusion

This work investigated the influence of lattice vibrations on the breathing transition and thermodynamic properties of MIL-53(A1). For that purpose, volume-frequency relations were determined for each normal mode. It was shown that most high-frequency vibrations ($>300 \text{ cm}^{-1}$) in MIL-53(A1) follow a general volume-frequency trend. At high and low unit cell volumes the vibrational frequency decreases for increasing unit cell volumes due to weakening of the covalent bonds, while for intermediate volumes the opposite behavior is observed, which is an effect of dispersion forces. As a result, most vibrational frequencies show a counterintuitive increase when the material undergoes a transition from the CP phase to the LP phase.

Furthermore, the low-frequency vibrations in the terahertz region were examined. It has become clear that only a few modes will influence the dynamics of the phase transformation. On the one hand, a large decrease in vibrational frequencies for increasing unit cell volumes

was observed for those modes showing rotations of the organic linker thereby triggering the CP-to-LP phase transformation at high temperatures. On the other hand, two soft modes were predicted showing the opposite volume-frequency trend, which originates from an internal strain induced by the volume change. These soft modes stabilize the CP phase structure at low temperatures and trigger the LP-to-CP phase transformation. In addition, several other modes with an interesting volume-frequency behavior were discovered such as those exhibiting trampoline-like motion of the linker, which may also play an important role in the breathing process.

Analytical expressions could be fitted to the volume-frequency relations, which allowed to derive several thermodynamic properties as a function of the volume and temperature such as the Helmholtz free energy profile, the specific heat capacity, the bulk modulus, and the volumetric thermal expansion. The results were in fair agreement with literature data, especially for the CP phase. However, the predicted bulk modulus and the volumetric thermal expansion coefficient of the LP phase were overestimated. We claimed that the too high values of the mentioned properties resulted from the contribution of the low-frequency vibrations exhibiting rotations of the organic linkers. In general, terahertz vibrations were found to influence the thermodynamic properties significantly. Subsequently, small errors in the predicted frequencies can cause large deviations in the thermodynamic properties, indicating the urge of highly accurate DFT calculations including a high degree of anharmonicities.

Acknowledgement: This work is supported by the Fund for Scientific Research Flanders (FWO), the Research Board of the Ghent University (BOF), and BELSPO in the frame of IAP/7/05. Other funds are provided by the European Union's Horizon 2020 research and innovation programme [consolidator ERC Grant Agreement No.647755 - DYNPOR (2015–2020)]. The computational resources and services used in this work were provided by the VSC (Flemish Supercomputer Center), funded by the Research Foundation – Flanders (FWO) and the Flemish Government – department EWI.

References

- [1] H.-C. Zhou, S. Kitagawa, Metal–organic frameworks (MOFs). *Chem. Soc. Rev.* **2014**, *43*, 5415.
- [2] G. Maurin, C. Serre, A. Cooper, G. Férey, The new age of MOFs and of their porous-related solids. *Chem. Soc. Rev.* **2017**, *46*, 3104.
- [3] P. Z. Moghadam, A. Li, S. B. Wiggin, A. Tao, A. G. Maloney, P. A. Wood, S. C. Ward, D. Fairen-Jimenez, Development of a Cambridge structural database subset: a collection of metal–organic frameworks for past, present, and future. *Chem. Mater.* **2017**, *29*, 2618.
- [4] C. E. Wilmer, M. Leaf, C. Y. Lee, O. K. Farha, B. G. Hauser, J. T. Hupp, R. Q. Snurr, Large-scale screening of hypothetical metal–organic frameworks. *Nature Chem.* **2012**, *4*, 83.
- [5] Y. Cui, B. Li, H. He, W. Zhou, B. Chen, G. Qian, Metal–organic frameworks as platforms for functional materials. *Acc. Chem. Res.* **2016**, *49*, 483.
- [6] Q. Yang, D. Liu, C. Zhong, J.-R. Li, Development of computational methodologies for metal–organic frameworks and their application in gas separations. *Chem. Rev.* **2013**, *113*, 8261.
- [7] F.-Y. Yi, D. Chen, M.-K. Wu, L. Han, H.-L. Jiang, Chemical sensors based on metal–organic frameworks. *ChemPlusChem.* **2016**, *81*, 675.
- [8] S. M. J. Rogge, A. Bavykina, J. Hajek, H. Garcia, A. I. Olivos-Suarez, A. Sepúlveda-Escribano, A. Vimont, G. Clet, P. Bazin, F. Kapteijn, M. Daturi, E. V. Ramos-Fernandez, F. X. Llabrés i Xamena, V. Van Speybroeck, J. Gascon, Metal–organic and covalent organic frameworks as single-site catalysts. *Chem. Soc. Rev.* **2017**, *46*, 3134.
- [9] S. Horike, S. Shimomura, S. Kitagawa, Soft porous crystals. *Nature Chem.* **2009**, *1*, 695.
- [10] A. Schneemann, V. Bon, I. Schwedler, I. Senkowska, S. Kaskel, R. A. Fischer, Flexible metal–organic frameworks. *Chem. Soc. Rev.* **2014**, *43*, 6062.
- [11] F.-X. Coudert, Responsive metal–organic frameworks and framework materials: under pressure, taking the heat, in the spotlight, with friends. *Chem. Mater.* **2015**, *27*, 1905.
- [12] L. Vanduyfhuys, S. M. J. Rogge, J. Wieme, S. Vandenbrande, G. Maurin, M. Waroquier, V. Van Speybroeck, Thermodynamic insight into stimuli-responsive behaviour of soft porous crystals. *Nature Commun.* **2018**, *9*, 204.
- [13] P. G. Yot, Z. Boudene, J. Macia, D. Granier, L. Vanduyfhuys, T. Verstraelen, V. Van Speybroeck, T. Devic, C. Serre, G. Férey, N. Stock, G. Maurin, Metal–organic frameworks as potential shock absorbers: the case of the highly flexible MIL-53(Al). *Chem. Commun.* **2014**, *50*, 9462.
- [14] P. Horcajada, C. Serre, G. Maurin, N. A. Ramsahye, F. Balas, M. Vallet-Regi, M. Sebban, F. Taulelle, G. Férey, Flexible porous metal-organic frameworks for a controlled drug delivery. *J. Am. Chem. Soc.* **2008**, *130*, 6774.
- [15] J. Wieme, K. Lejaeghere, G. Kresse, V. Van Speybroeck, Tuning the balance between dispersion and entropy to design temperature-responsive flexible metal-organic frameworks. *Nature Commun.* **2018**, *9*, 4899.
- [16] P. Freund, L. Mielewczyk, M. Rauche, I. Senkowska, S. Ehrling, E. Brunner, S. Kaskel, MIL-53(Al)/carbon films for CO₂-sensing at high pressure. *ACS Sustain. Chem. Eng.* DOI: 10.1021/acssuschemeng.8b05368.
- [17] T. Loiseau, C. Serre, C. Huguénard, G. Fink, F. Taulelle, M. Henry, T. Bataille, G. Férey, A rationale for the large breathing of the porous aluminum terephthalate (MIL-53) upon hydration. *Chem. Eur. J.* **2004**, *10*, 1373.
- [18] Y. Liu, J.-H. Her, A. Dailly, A. J. Ramirez-Cuesta, D. A. Neumann, C. M. Brown, Reversible structural transition in MIL-53 with large temperature hysteresis. *J. Am. Chem. Soc.* **2008**, *130*, 11813.

- [19] A. Boutin, M.-A. Springuel-Huet, A. Nossou, A. Gédéon, T. Loiseau, C. Volkringer, G. Férey, F.-X. Coudert, A. H. Fuchs, Breathing transitions in MIL-53(Al) metal–organic framework upon xenon adsorption. *Angew. Chem. Int. Ed.* **2009**, *48*, 8314.
- [20] F.-X. Coudert, A. Boutin, A. H. Fuchs, A. V. Neimark, Adsorption deformation and structural transitions in metal–organic frameworks: from the unit cell to the crystal. *J. Phys. Chem. Lett.* **2013**, *4*, 3198.
- [21] M. R. Ryder, B. Civalleri, T. D. Bennett, S. Henke, S. Rudić, G. Cinque, F. Fernandez-Alonso, J.-C. Tan, Identifying the role of terahertz vibrations in metal–organic frameworks: from gate-opening phenomenon to shear-driven structural destabilization. *Phys. Rev. Lett.* **2014**, *113*, 215502.
- [22] M. R. Ryder, B. Civalleri, G. Cinque, J.-C. Tan, Discovering connections between terahertz vibrations and elasticity underpinning the collective dynamics of the HKUST-1 metal–organic framework. *CrystEngComm.* **2016**, *18*, 4303.
- [23] A. Krylov, A. Vtyurin, P. Petkov, I. Senkowska, M. Maliuta, V. Bon, T. Heine, S. Kaskel, E. Slyusareva, Raman spectroscopy studies of the terahertz vibrational modes of a DUT-8(Ni) metal–organic framework. *Phys. Chem. Chem. Phys.* **2017**, *19*, 32099.
- [24] A. E. J. Hoffman, L. Vanduyfhuys, I. Nevjestic, J. Wieme, S. M. J. Rogge, H. Depauw, P. Van Der Voort, H. Vrielinck, V. Van Speybroeck, Elucidating the vibrational fingerprint of the flexible metal–organic framework MIL-53(Al) using a combined experimental/computational approach. *J. Phys. Chem. C* **2018**, *122*, 2734.
- [25] A. M. Walker, B. Civalleri, B. Slater, C. Mellot-Draznieks, F. Corà, C. M. Zicovich-Wilson, G. Román-Pérez, J. M. Soler, J. D. Gale, Flexibility in a metal–organic framework material controlled by weak dispersion forces: the bistability of MIL-53(Al). *Angew. Chem. Int. Ed.* **2010**, *49*, 7501.
- [26] A. Erba, On combining temperature and pressure effects on structural properties of crystals with standard ab initio techniques. *J. Chem. Phys.* **2014**, *141*, 124115.
- [27] E. Cockayne, Thermodynamics of the flexible metal–organic framework material MIL-53(Cr) from first-principles. *J. Phys. Chem. C* **2017**, *121*, 4312.
- [28] G. Kresse, J. Furthmüller, Efficient iterative schemes for ab initio total-energy calculations using a plane-wave basis set. *Phys. Rev. B* **1996**, *54*, 11169.
- [29] J. P. Perdew, K. Burke, M. Ernzerhof, Generalized gradient approximation made simple. *Phys. Rev. Lett.* **1996**, *77*, 3865.
- [30] S. Grimme, J. Antony, S. Ehrlich, H. Krieg, A consistent and accurate ab initio parametrization of density functional dispersion correction (DFT-D) for the 94 elements H–Pu. *J. Chem. Phys.* **2010**, *132*, 154104.
- [31] S. Grimme, S. Ehrlich, L. Goerigk, Effect of the damping function in dispersion corrected density functional theory. *J. Comput. Chem.* **2011**, *32*, 1456.
- [32] P. E. Blöchl, Projector augmented-wave method. *Phys. Rev. B* **1994**, *50*, 17953.
- [33] G. Kresse, D. Joubert, From ultrasoft pseudopotentials to the projector augmented-wave method. *Phys. Rev. B* **1999**, *59*, 1758.
- [34] H. J. Monkhorst, J. D. Pack, Special points for Brillouin-zone integrations. *Phys. Rev. B* **1976**, *13*, 5188.
- [35] D. E. P. Vanpoucke, K. Lejaeghere, V. Van Speybroeck, M. Waroquier, A. Ghysels, Mechanical properties from periodic plane wave quantum mechanical codes: The challenge of the flexible nanoporous MIL-47(V) framework. *J. Phys. Chem. C* **2015**, *119*, 23752.
- [36] A. Ghysels, T. Verstraelen, K. Hemelsoet, M. Waroquier, V. Van Speybroeck, TAMkin: a versatile package for vibrational analysis and chemical kinetics. *J. Chem. Inf. Model.* **2010**, *50*, 1736.
- [37] S. Baroni, S. De Gironcoli, A. Dal Corso, P. Giannozzi, Phonons and related crystal properties from density-functional perturbation theory. *Rev. Mod. Phys.* **2001**, *73*, 515.
- [38] X. Wu, D. Vanderbilt, D. R. Hamann, Systematic treatment of displacements, strains, and electric fields in density-functional perturbation theory. *Phys. Rev. B* **2005**, *72*, 035105.
- [39] A. Erba, M. Shahrokhi, R. Moradian, R. Dovesi, On how differently the quasi-harmonic approximation works for two isostructural crystals: thermal properties of periclase and lime. *J. Chem. Phys.* **2015**, *142*, 044114.
- [40] C. Serre, S. Bourrelly, A. Vimont, N. A. Ramsahye, G. Maurin, P. L. Llewellyn, M. Daturi, Y. Filinchuk, O. Leynaud, P. Barnes, G. Férey, An explanation for the very large breathing effect of a metal–organic framework during CO₂ adsorption. *Adv. Mater.* **2007**, *19*, 2246.
- [41] J. Salazar, G. Weber, J. Simon, I. Bezverkhy, J. Bellat, Characterization of adsorbed water in MIL-53(Al) by FTIR spectroscopy and ab-initio calculations. *J. Chem. Phys.* **2015**, *142*, 124702.
- [42] M. R. Ryder, B. Van de Voorde, B. Civalleri, T. D. Bennett, S. Mukhopadhyay, G. Cinque, F. Fernandez-Alonso, D. De Vos, S. Rudić, J.-C. Tan, Detecting molecular rotational dynamics complementing the low-frequency terahertz vibrations in a zirconium-based metal–organic framework. *Phys. Rev. Lett.* **2017**, *118*, 255502.
- [43] S. M. J. Rogge, M. Waroquier, V. Van Speybroeck, Reliably modeling the mechanical stability of rigid and flexible metal–organic frameworks. *Acc. Chem. Res.* **2017**, *51*, 138.
- [44] J. P. S. Mowat, V. R. Seymour, J. M. Griffin, S. P. Thompson, A. M. Z. Slawin, D. Fairen-Jimenez, T. Düren, S. E. Ashbrook, P. A. Wright, A novel structural form of MIL-53 observed for the scandium analogue and its response to temperature variation and CO₂ adsorption. *Dalton Trans.* **2012**, *41*, 3937.
- [45] R. Demuyne, S. M. J. Rogge, L. Vanduyfhuys, J. Wieme, M. Waroquier, V. Van Speybroeck, Efficient construction of free energy profiles of breathing metal–organic frameworks using advanced molecular dynamics simulations. *J. Chem. Theory Comput.* **2017**, *13*, 5861.
- [46] P. Vinet, J. Ferrante, J. H. Rose, J. R. Smith, Compressibility of solids. *J. Geophys. Res.* **1987**, *92*, 9319.
- [47] F. A. Kloutse, R. Zacharia, D. Cossement, R. Chahine, Specific heat capacities of MOF-5, Cu-BTC, Fe-BTC, MOF-177 and MIL-53(Al) over wide temperature ranges: measurements and application of empirical group contribution method. *Microporous Mesoporous Mater.* **2015**, *217*, 1.
- [48] C. Nanthamathee, S. Ling, B. Slater, M. P. Atfield, Contrast distinct thermoresponsive behavior of isostructural MIL-53 type metal–organic frameworks by modifying the framework inorganic anion. *Chem. Mater.* **2014**, *27*, 85.
- [49] S. M. J. Rogge, L. Vanduyfhuys, A. Ghysels, M. Waroquier, T. Verstraelen, G. Maurin, V. Van Speybroeck, A comparison of

barostats for the mechanical characterization of metal–organic frameworks. *J. Chem. Theory Comput.* **2015**, *11*, 5583.

[50] L. Wang, C. Wang, Y. Sun, K. Shi, S. Deng, H. Lu, Large negative thermal expansion provided by metal-organic framework MOF-5: a first-principles study. *Mater. Chem. Phys.* **2016**, *175*, 138.

[51] V. Barone, M. Biczysko, J. Bloino, Fully anharmonic IR and Raman spectra of medium-size molecular systems: accuracy and interpretation. *Phys. Chem. Chem. Phys.* **2014**, *16*, 1759.

[52] M. T. Ruggiero, J. A. Zeitler, A. Erba, Intermolecular anharmonicity in molecular crystals: interplay between experimental low-frequency dynamics and quantum quasi-harmonic simulations of solid purine. *Chem. Commun.* **2017**, *53*, 3781.

Supplementary Material: The online version of this article offers supplementary material (<https://doi.org/10.1515/zkri-2018-2154>).